Gram-Scale Synthesis of Catalytic Co_9S_8 Nanocrystal Ink as a Cathode Material for Spray-Deposited, Large-Area Dye-Sensitized Solar Cells

Shu-Hao Chang,[†] Ming-De Lu,[‡] Yung-Liang Tung,[‡] and Hsing-Yu Tuan[†,*]

[†]Department of Chemical Engineering, National Tsing Hua University, 101, Section 2, Kuang-Fu Road, Hsinchu, Taiwan 30013, ROC and [‡]Green Energy & Environment Research Laboratories, Industrial Technology Research Institute, 195, Sec. 4, Chung Hsing Road, Chutung, Hsinchu, Taiwan 31040, ROC

ABSTRACT We report the development of Co_9S_8 nanocrystals as a cost-effective cathode material that can be readily combined with spraying techniques to fabricate large-area dye-sensitized solar cell (DSSC) devices and can be further connected with series or parallel cell architectures to obtain a relatively high output voltage or current. A gram-scale synthesis of Co_9S_8 nanocrystal is carried out *via* a noninjection reaction by mixing anhydrous $CoCl_2$ with trioctylphosphine (TOP), dodecanethiol and oleylamine (OLA) at 250 °C. The Co_9S_8 nanocrystals possess excellent catalytic ability with respect to I^-/I_3^- redox reactions. The Co_9S_8 nanocrystals are prepared as nanoinks to fabricate uniform, crack-free Co_9S_8 thin films on different substrates by using a spray deposition technique. These Co_9S_8 films are used as counter electrodes assembled with dye-adsorbed TiO_2 photoanodes to fabricate DSSC devices having a working area of 2 cm^2 and an average power conversion efficiency (PCE) of 7.02 ± 0.18% under AM 1.5 solar illumination, which is comparable with the PCE of 7.2 ± 0.12% obtained using a Pt cathode. Furthermore, six 2 cm^2-sized DSSC devices connected in series output an open-circuit voltage of 4.2 V that can power a wide range of electronic devices such as LED arrays and can charge commercial lithium ion batteries.

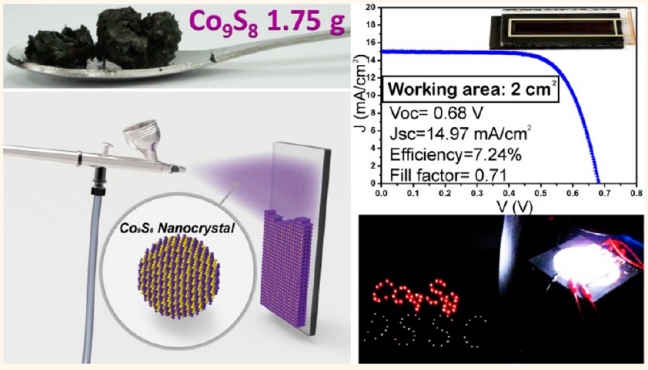

KEYWORDS: cobalt sulfide · nanocrystals · cost-effective · large area · dye-sensitized solar cell · counter electrode

Ligand-stabilized colloidal nanocrystals exhibit stabile dispersibility in solvents while strong solvation of the ligand's tails generates a sufficient repulsive force against interparticle attraction that prevents sedimentation. The morphology of nanocrystals can be also controlled in the colloid synthetic chemistry.[1−3] Functional large-area device layers can be deposited from nanocrystal solutions, the so-called nanocrystal inks, using solution-based printing techniques, including spray deposition, blade coating, spin coating and drop casting. Device layers can be made *via* roll-to-roll, high-throughput (>20 m/min), and large-area (>150 m^2/h) solution-processed strategies using an established production line operated with a given set of parameters that is not achievable using vacuum-based deposition techniques. Complex devices made by assembly of nanostructure on various substrates can be also constructed.[4−6]

Platinum (Pt) is the most commonly used cathode material for dye-sensitized solar cell (DSSC) because of its high conductivity, stability and catalytic activity with respect to iodine/triiodide (I^-/I_3^-) reduction.[7] However, the use of Pt is limitedly by its high cost. Thermal decomposition, sputtering, and electrochemical deposition are widely used for fabricating Pt counter electrodes.[8−10] However, the high-energy-consuming procedure works against the advantage of cost effectiveness. Inorganic nanomaterials outperform bulk micrometer-sized powders with respect to many catalytic reactions because of their significantly large exposure areas and can potentially serve as Pt-alternatives for a

* Address correspondence to hytuan@che.nthu.edu.tw.

Received for review August 15, 2013 and accepted August 31, 2013.

Published online August 31, 2013
10.1021/nn404272j

DSSC[7,11−13] or a quantum dot-sensitized solar cell (QDSSC).[14] Inorganic nanomaterials, including metal oxides,[15] metal nitrides,[15−17] metal chalcogenides[18−21] and composite structures,[22−24] have been found to have catalytic ability comparable to that of Pt with respect to I^-/I_3^- redox reactions.

Metal chalcogenides nanomaterials represent important parts of topics being researched and are used in a wide range of applications.[25−31] Co_9S_8 is a particularly good hydrodesulfurization (HDS) catalyst with excellent activity for the oxygen reduction reaction (ORR) under acidic conditions.[32,33] Co_9S_8 has a face-centered cubic (fcc) structure in the space group of $Fm\bar{3}m$ (225) with a lattice constant of 9.928 ± 0.001 Å.[34] Because Co_9S_8 has a narrow homogeneity range and usually forms peritectically at high temperatures (~835 °C),[35] the reaction conditions (*e.g.*, reaction temperature and reaction time) are highly dependent on the formation of pure Co_9S_8. The bonding modes between metal and sulfur are typically complex and result in an intricate crystal structure.[36] Binary cobalt sulfides exist in the form of various crystalline phases in a wide range of stoichiometries, including CoS, CoS_2, Co_3S_4, and Co_9S_8, and in nonstoichiometric $Co_{1-x}S$.[37] The other challenge for forming pure Co_9S_8 is that the cobalt ion easily reacts with oxygen to form cobalt oxide or other cobalt-compound impurities.[38] Thus far, there have been few reports on the synthesis of Co_9S_8 nanocrystals and many of these are based on two-step sulfuration reactions.[39−41] For instance, Alivisatos *et al.* fabricated hollow Co_9S_8 nanocrystals by first forming cobalt nanocrystals followed by a sulfuration process.[39] Recently, Co_9S_8−oleylamine hybrid nanosheets have been synthesized *via* an in-plane coassembly process.[41] However, it is still challenging to use a one-step process for the synthesis of a considerably large amount of high-quality colloid Co_9S_8 nanocrystals to meet application requirements. Furthermore, their performance with respect to their application to DSSC cathodes has not been investigated.

In this study, high-quality Co_9S_8 nanocrystals in gram-scale production are synthesized by a noninjection, one-pot reaction at ~250 °C. On the basis of the analysis of cyclic voltammetry data and the Tafel curve, we find that the Co_9S_8 nanocrystal cathode has excellent catalytic ability with respect to I^-/I_3^- redox reactions, thereby proving that these nanocrystals are a promising avenue as cathode material for DSSCs. The nanocrystals exhibit stable dispersion in various nonpolar solvents that matches well with the criteria of nanocrystal inks. The nanocrystal inks are spray-deposited on various conductive substrates by an air-brush to fabricate uniform, large-area (~100 cm^2) micrometer-thick films. For device performance evaluation, the DSSC devices are fabricated with a 2 cm^2 (0.5 cm × 4 cm) working area, which is at least 5 times larger than the working areas (0.15−0.4 cm^2) of the cells usually evaluated in the literature. The champion power conversion efficiency (PCE) of Co_9S_8/Mo counter electrode in our DSSC system is 7.24% under AM1.5 illumination, which is comparable to that of Pt with a PCE of 7.34%. The single cell delivers a short-circuit current of more than 28 mA with an open-circuit voltage of ~0.7 V, which is sufficient to drive electric devices. Higher voltage (>3 V) DSSC devices composed of six 2 cm^2 cells connected in series are also applied to turn on devices requiring higher operation voltages.

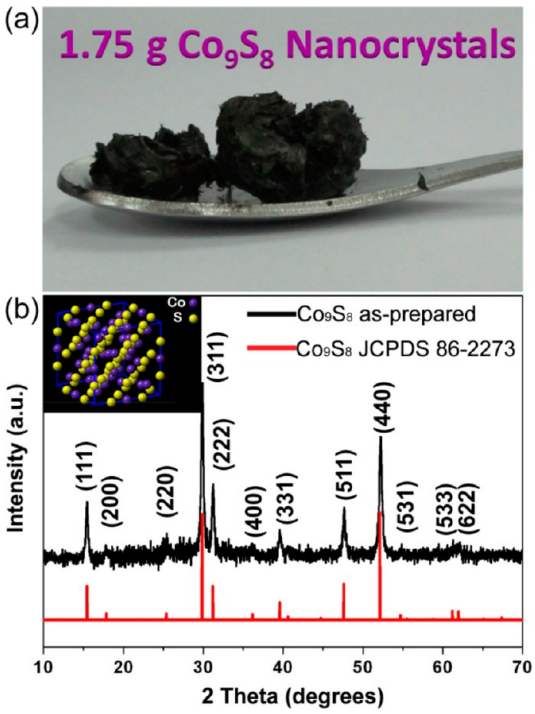

Figure 1. (a) Photograph of 1.75 g of Co_9S_8 nanocrystal powder; (b) XRD pattern of Co_9S_8 nanocrystal product and the inset shows the unit cell of FCC cobalt sulfide.

RESULTS AND DISCUSSION

A noninjection, one-pot reaction was conducted as the synthetic approach for the production of Co_9S_8 nanocrystals since this method can be easily scaled up to obtain large quantities of the products. Co_9S_8 nanocrystals were prepared by combining a mixture of anhydrous $CoCl_2$ with trioctylphosphine (TOP), dodecanethiol and oleylamine (OLA) at room temperature in an Ar atmosphere. Dodecanethiol served as the sulfur source[42,43] and reduced the sulfuration temperature with cobalt precursors.[44] The mixture was heated to 250 °C and was held at this temperature for 10 min. During this period, the color changed from blue (anhydrous cobalt(II) chloride) to dark black, indicating the formation of Co_9S_8 nanocrystals. One batch reaction could produce more than 1 g of the product with a yield of more than 90% (Figure 1a). The X-ray diffraction (XRD) result shown in Figure 1b indicates the as-prepared sample with peaks indexed perfectly with the Co_9S_8 FCC phase (JCPDS No. 86-2273) having the cell

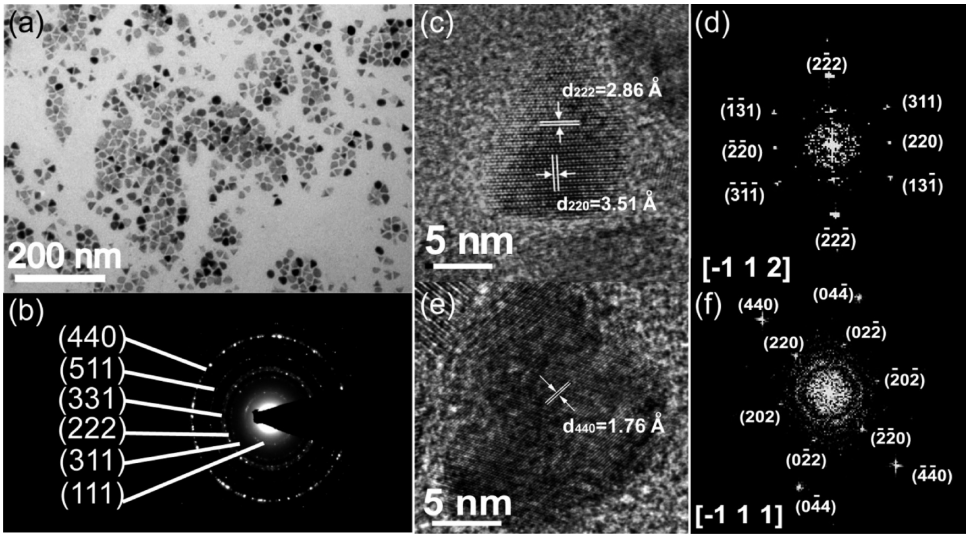

Figure 2. (a) TEM image of cobalt sulfide nanocrystals and (b) their corresponding SAED pattern; (c−f) HRTEM images of cobalt sulfide nanocrystals and their corresponding FFT pattern.

parameter a = 9.92 Å. The inset of Figure 1b shows the unit cell of FCC Co_9S_8.

Co_9S_8 nanocrystals had facet shapes with an average particle size of ~18 nm as observed by transmission electron microscopy (TEM) (Figure 2a). The selected area electron diffraction (SAED) pattern (Figure 2b) verified that product was FCC Co_9S_8. Figure 2c−f shows HRTEM images with the associated fast Fourier transform (FFT) of Co_9S_8 nanocrystals. These nanoparticles had lattice fringe corresponding to Co_9S_8 and exhibited excellent crystallinity. The corresponding reciprocal lattice image could be indexed to the [−112] and [−111] zone axes of fcc Co_9S_8. From Figure 2c, the interfringe distance of 0.286 and 0.351 nm corresponds to the (222) and (220) planes of the cubic Co_9S_8 phase, respectively. Further, the clear crystal fringe of 0.176 nm shown in Figure 2e was indexed for the (440) planes of Co_9S_8. Energy-dispersive X-ray spectroscopy (EDS) obtained from fields of nanocrystals indicated an average Co/S composition of 9:8, confirming the stoichiometry of Co_9S_8 (Figure 3a). X-ray photoelectron spectroscopy (XPS) is a surface-sensitive tool used for analyzing the chemical state of cobalt sulfide. The binding energy was corrected by referencing C 1s (284.60 eV). The measured cobalt 2p peaks were located at 778.5 and 793.9 eV, and the Co 2p spectrum had small asymmetric core electron peaks, which were identical with the literature value.[45,46] The measured S 2p peaks were located at 161.2 and 162.3 eV with a split of 1.1 eV; this was in good agreement with the previous report.[47]

The Co_9S_8 nanocrystals exhibited stable solvent dispersion at high nanocrystal concentrations (>20 mg/mL) without sedimentation for several months in many nonpolar solvents. The Co_9S_8 nanoinks can be carried by the inert gas traveling through the inkjet nozzle and sprayed onto the substrate to form a thin film. Figure 4a depicts a sketch of the spraying experimental setup. (see Movie S1 in the Supporting Information for fabrication process). In the case of spray deposition, the film quality is associated with nozzle geometry, ink properties, substrate temperature and the pressure of the process gas.[48] The dispersion stability of inks is critical for this process. If a nanoink is not stable, the inkjet nozzles get clogged frequently by the aggregated particles, which results in unstable ejection. Figure 4b shows a photograph of Co_9S_8 nanocrystals dispersed in hexane at a concentration of 20 mg/mL. FTO- and Mo-coated glasses were used as substrates for the Co_9S_8 nanocrystal deposition. A 100 cm^2 uniform film composed of spray-deposited Co_9S_8 nanocrystals was fabricated in 5 min by spraying the inks (Figure 4c). The as-deposited films were annealed at 350 °C in an Ar atmosphere for 2 h. This annealing procedure improved mechanical strength and adhesion to the substrates; furthermore, the surfactants that were capped on the Co_9S_8 nanocrystal surface could be removed to increase conductivity and crystallinity without any phase change. (Figure S1 in the Supporting Information for XRD characterization). Figure 4d shows the cross-sectional and the plan view of the annealed Co_9S_8 film. The scanning electron microscopy (SEM) images revealed that the film was dense and no obvious crack was formed. The thickness of the cobalt sulfide layer was in the range of 0.9−1.2 μm, which could be controlled by tuning the concentration of nanoinks, pressure of the carrier gas and the spraying time. The Co_9S_8 nanocrystals were also deposited on the Mo substrates; the cross-sectional image of the Co_9S_8 film is shown in Figure S2 in the Supporting Information.

In our system, I^-/I_3^- redox couple was considered as a redox mediator. The nanocrystal films had more reaction sites for I^-/I_3^- reduction reactions in the electrolyte because of the large specific surface area

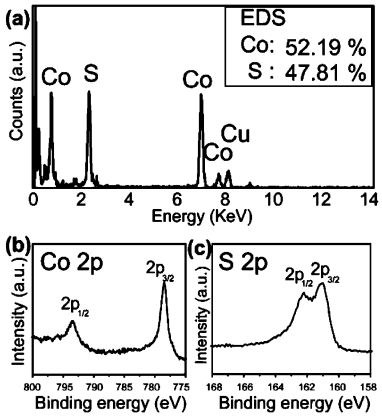

Figure 3. (a) EDS result of cobalt sulfide nanocrystals and XPS results of cobalt sulfide nanocrystals for (b) Co 2p region and (c) S 2p region, respectively.

which increased effective active area.[49] Figure 5a shows the cyclic voltammograms in an acetonitrile solution with 10.0 mM LiI, 1.0 mM I_2, and 0.1 M $LiClO_4$ for Pt, Co_9S_8 on FTO substrate (Co_9S_8/FTO), and Co_9S_8 on Mo substrate (Co_9S_8/Mo) at a scanning rate of 20 mV/s. Two pairs of oxidation and reduction peaks were predominantly observed in three curves. The result indicated that both cobalt sulfide and Pt had good electrocatalytic activity for the I^-/I_3^- system. The anodic peaks shown in Figure 5a are denoted as (I) and (II), and the reverse cathode peaks are denoted as (I′) and (II′), respectively. According to the literature,[50] iodine is oxidized to triiodide (peak I) and then to iodine (peak II) by reactions 1 and 2, respectively.

$$3I^- \rightarrow I_3^- + 2e^- \quad (1)$$

$$2I_3^- \rightarrow 3I_2 + 2e^- \quad (2)$$

In the reverse process, iodine is first reduced to triiodide (peak II′), then to iodide (peak I′) corresponding to the reactions 3 and 4, respectively.

$$3I_2 + 2e^- \rightarrow 2I_3^- \quad (3)$$

$$I_3^- + 2e^- \rightarrow 3I^- \quad (4)$$

The current density of the oxidation and reduction for three electrodes was almost identical. This suggested that the electrocatalytic ability of Co_9S_8 toward I^-/I_3^- redox couple was comparable to that of Pt. It is explained that the charge-transfer resistance in the I^-/I_3^- redox reaction for the three electrodes was very close. The electrocatalytic ability was reconfirmed by a Tafel polarization measurement, which is a powerful electrochemical characterization method for examining the interfacial charge-transfer properties on the electrode surface. The Tafel curve can be separated into three zones: polarization zone (low potential), Tafel zone (intermediate potential with a sharp slope),

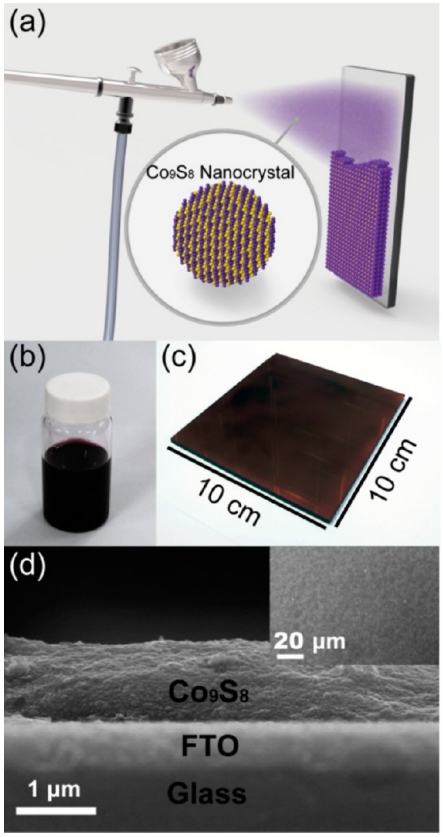

Figure 4. (a) Schematic diagram for the spray deposition of Co_9S_8 nanocrystals on a substrate; (b) photograph Co_9S_8 nanoink used for thin-film deposition; (c) photograph of Co_9S_8 nanocrystal thin film on a 10 cm × 10 cm FTO glass; (d) SEM image of the Co_9S_8 film/FTO showing the cross-sectional and the plan view (inset), respectively. Movie S1 in the Supporting Information provides the fabrication process of spray-deposited Co_9S_8 thin film.

and diffusion zone (high potential). The Tafel polarization curves by symmetrical dummy cell are shown in figure 5b. In the Tafel zone, both Co_9S_8/Mo and Co_9S_8/FTO exhibited a little larger exchange current density (J_0) than the Pt electrode, which could be obtained by intersecting the cathodic branch and the equilibrium potential line (Figure S3 in the Supporting Information). The R_{ct} value could be calculated using eq 5,[51]

$$J_0 = \frac{RT}{nFR_{ct}} \quad (5)$$

where R denotes the gas constant; T, the temperature; F, Faraday's constant; n, the total number of electrons involved in the reaction; and R_{ct}, the charge transfer resistance. Using this equation, we found that the R_{ct} value of Pt was a little larger than that of Co_9S_8/Mo and Co_9S_8/FTO.

The DSSC devices had a working area of 2 cm^2 (4 cm × 0.5 cm) and used the Co_9S_8 layer as the cathode and the N719 adsorbed mesoporous TiO_2 film as the anode. Figure 6a shows a photograph of a 2 cm^2 DSSC device. Figure 6b shows the $J-V$ curves of the DSSC using Pt, Co_9S_8/FTO and Co_9S_8/Mo counter

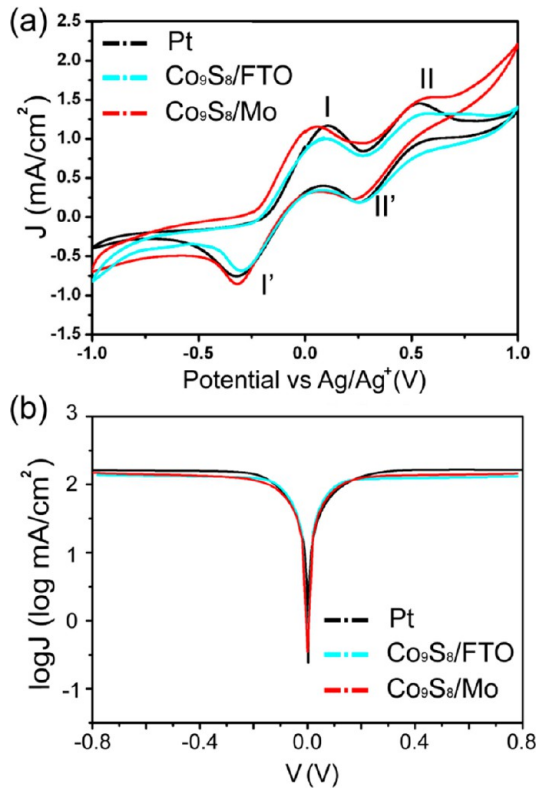

Figure 5. (a) Cyclic voltammograms of the Pt, Co_9S_8 on FTO substrate, and Co_9S_8 on Mo substrate for I^-/I_3^- species. The peak I and peak I′ represent $3I^- \leftrightarrow I_3^- + 2e^-$; peak II and peak II′ represent $2I_3^- \leftrightarrow 3I_2 + 2e^-$, respectively. (b) Tafel polarization curves of the I^-/I_3^- symmetrical cells of the Pt on FTO substrate, Co_9S_8 on FTO substrate, and Co_9S_8 on Mo substrate.

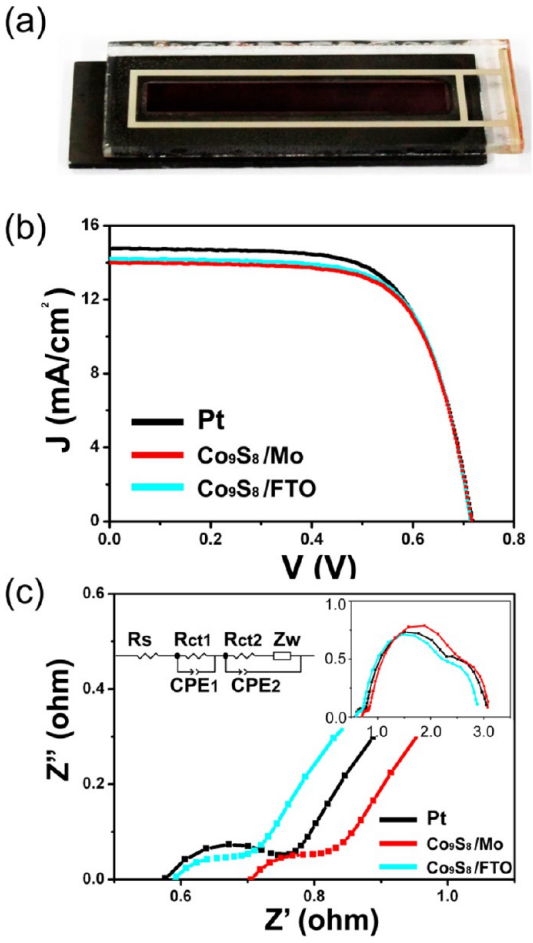

Figure 6. (a) Photograph of a DSSC cell with 2 cm^2 working area; (b) $J-V$ curves of the DSSCs with the Pt, Co_9S_8 on FTO, and Co_9S_8 on Mo counter electrode measured under AM1.5 illumination; (c) Nyquist plots of DSSCs with the Pt, Co_9S_8 on FTO, and Co_9S_8 on Mo counter electrode.

electrodes. The photovoltaic parameters are summarized in the Table 1. Under the completely same experimental conditions, the catalytic ability between Co_9S_8/FTO and Co_9S_8/Mo was found to be similar, and the slight differences between the two electrodes attributed to the uniformity of Co_9S_8 film. The Co_9S_8/FTO−DSSC and Co_9S_8/Mo−DSSC yielded power conversion efficiencies (PCEs) of 6.91% and 7.00% under AM 1.5 illumination, respectively. The results were a slightly lower than those obtained for the Pt PCE. The open-circuit voltage (V_{oc}) values of the three cells were around 0.71−0.72 V. However, the fill factors of Pt-DSSC were smaller than those of the others, which was attributed to the larger R_{ct}. The short-circuit current density (J_{sc}) values of Co_9S_8/FTO−DSSC and Co_9S_8/Mo−DSSC were slightly lower than those of Pt−DSSC. An electrochemical impedance spectroscopy (EIS) measurement was also conducted to investigate the catalytic activity and the impedance of the DSSC. To evaluate the electrochemical characteristics of three counter electrodes, the EIS plots were fitted using an equivalent circuit model shown in the inset of Figure 6c.[52,53] In the plot, three semicircles were clearly observed, which were obtained by changing the frequency from 10^5 to 10^{-2} Hz. The left most arch was

TABLE 1. Photovoltaic Performances of DSSCs Using Pt, Co_9S_8/FTO, and Co_9S_8/Mo as Counter Electrodes

	V_{oc} (V)	J_{sc} (mA/cm^2)	FF	PCE (%)	R_s (Ω)	R_{ct1}(Ω)
Pt	0.72	14.75	0.67	7.13	0.58	0.17
Co_9S_8/FTO	0.71	14.21	0.69	7.00	0.59	0.14
Co_9S_8/Mo	0.72	13.98	0.69	6.91	0.71	0.13

considered the charge transfer resistance (R_{ct1}) at the counter electrode/electrolyte interface and the corresponding double layer capacitance (C_{dl1}) of the electrolyte/counter electrode interface. The R_{ct1} values of Co_9S_8/FTO and Co_9S_8/Mo were found to be 0.14 and 0.13 Ω, respectively, which were close to value of 0.17 Ω for a Pt electrode. Typically, the redox reaction at the counter electrode/electrolyte interface can divided into three stages:[54] (1) the I_3^- diffusion from the bulk solution to the vicinity of counter electrode, (2) the adsorption of I_3^- on the surface of the counter electrode, and (3) the charge transfer from and the I^- removal from the surface of the counter electrode. The rate of the redox reaction was significantly

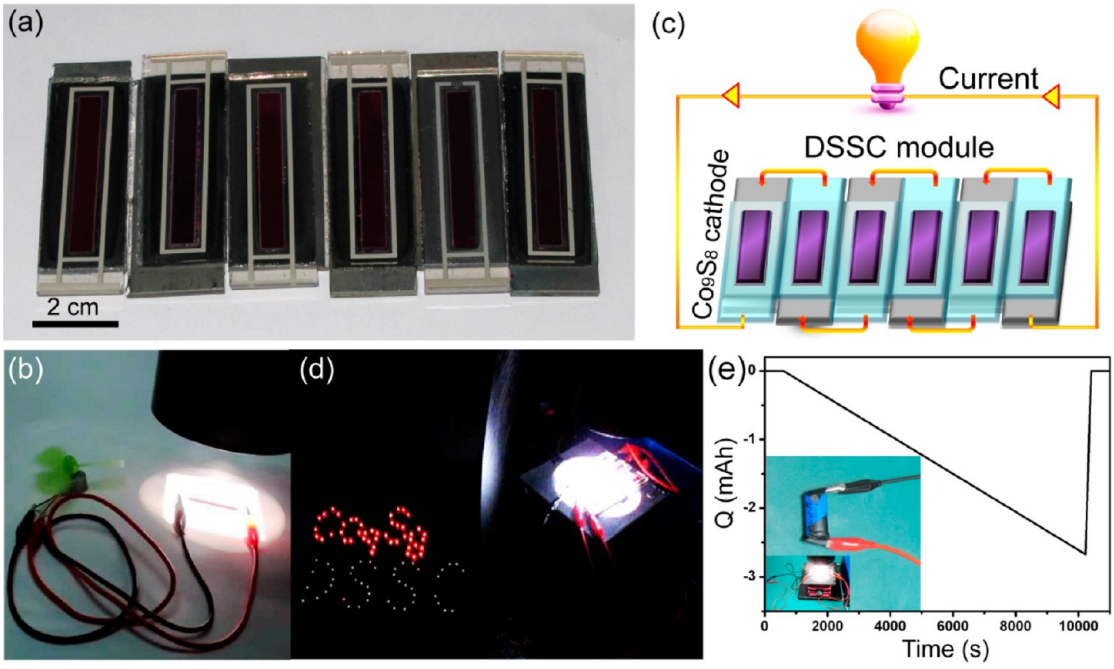

Figure 7. (a) Photograph of six 2 cm^2-sized DSSC cells; (b) an electric fan turned on by single DSSC; (c) schematic diagram of six series-connected DSSCs; (d) LED arrays lit by the six series-connected DSSCs; (e) LIB charged by the six series-connected DSSCs and its discharge $Q-t$ curve. Movies S2 and S3 in the Supporting Information show the handling of DSSCs with a Co_9S_8 cathode to power an electric fan and LED bulbs, respectively.

influenced by the effective active site at which the Co_9S_8 films might be larger than the Pt film. Therefore, the charge-transfer resistance at the Co_9S_8/Mo and Co_9S_8/FTO counter electrodes/electrolyte interface was smaller than that obtained in the case of Pt in our experiment. More PCEs values obtained from Co_9S_8/Mo−DSSC and Co_9S_8/FTO−DSSC under similar conditions are listed in the Supporting Information. The DSSC device with a Co_9S_8 nanocrystal counter electrode exhibited the highest PCE of 7.24% with an average value of 7.02 ± 0.18%.

The DSSC cells (Figure 7a) were used for powering a wide range of electronic devices. The 2 cm^2-DSSC device produced a short-circuit current of more than 28 mA, which is sufficient to turn on an electric fan (Figure 7b). The electric fan remains running while the cell is under continuous illumination (see Movie S2 in the Supporting Information). However, most of the electronic devices cannot be powered by this low voltage (~0.6 V). Six DSSCs with Co_9S_8 electrodes were connected in series to achieve an open circuit voltage of 4.2 V (Figure 7c). This series-connected DSSC devices could directly power numerous electronic devices, for example, calculators (1.5 V), yellow and red LEDs (2 V), and remote controllers (3 V), and charge lithium ion batteries (LIBs) (>3.5 V). As a demonstration, LED arrays containing more than 90 LED bulbs were lit without fading in real time by the DSSC devices as shown in Figure 7d (see Movie S3 in the Supporting Information). The series-connected DSSC devices could charge energy storage devices. An empty commercial LIB (Model: 16340, 880 mAh) with a voltage of 2.8 V was charged by 6 DSSCs for 30 min until the voltage increased to 3.3 V. Then, it was discharged by using a potentiostat system (VMP3); the discharge $Q-t$ curve is shown in Figure 7e. A capacity of approximately 3 mAh was obtained, which was considerably smaller than the expected value of 12−14 mAh. The reason for the low capacity was the large resistance in LIB that consumed some energy. Therefore, DSSC devices using Co_9S_8 cathodes could potentially be extended to systems having a parallel connection of large area cells (>100 cm^2) to obtain high current of more than 1.5 A for high-rate charging. On the other hand, modules with more than 25 series-connected cells can achieve a high voltage of 12 V to drive automobile starter motors.

CONCLUSION

Gram-scale Co_9S_8 nanocrystal synthesis was achieved using a facile noninjection one-pot approach. The Co_9S_8 nanocrystals exhibited highly catalytic properties with respect to I^-/I_3^- redox reactions which has made them excellent for use as cathode materials for DSSC. The well-dispersed Co_9S_8 nanocrystal inks could be spray-deposited on different substrates to create dense cathode films for DSSC applications. The spray printing process could be used for fabricating a large-area nanocrystal film on substrates at a roll-to-roll process at a speed of up to 20 m/min. Single 2 cm^2-sized DSSC using Co_9S_8 counter electrodes assembled with TiO_2 photoanodes gave an average PCE of 7.02 ± 0.18% that was comparable to the value of 7.2 ± 0.12% obtained in the case of the Pt electrodes. We described

the performance of series-connected DSSCs to power electric fans, light up LED arrays, and charge energy storage devices. In the future, a coordinated design of DSSC modules can be developed to achieve higher output voltage and higher output current for a wide range of applications. This study advances the development of catalytic Co_9S_8 nanocrystal inks which hold immense potential as a cost-effective cathode material for large-area, solution-based processing DSSC module applications.

MATERIALS AND METHODS

Materials. All chemicals were used as received from the Aldrich chemical, including cobalt(II) chloride ($CoCl_2$, anhydrous 97%), trioctylphosphine ($[CH_3(CH_2)_7]_3P$, 90%), dodecanethiol ($C_{12}H_{25}SH$, >98%), oleylamine ($CH_3(CH_2)_7CH{=}CH(CH_2)_7CH_2NH_2$, 70%), hexane, and ethanol (ACS reagent grade, >99.5%).

Cobalt Sulfide Nanocrystal Synthesis. In the synthesis of Co_9S_8 nanocrystals, 5 mL of TOP and 0.25 mmol of $CoCl_2$ (0.0328g) were added to a 50 mL three-neck flask placed on a heating plate; one neck was connected to a temperature sensor and stopcock valve was connected to a Schlenk line system; the other neck was sealed by a rubber septum. Next, 5 mL of dodecanethiol and 5 mL of oleylamine (OLA) were injected into the three-neck flask with intensely stirring. The three-neck flask was purged using argon for 35 min. The temperature of reaction was instantly raised to 250 °C, which was kept at 250 °C for 10 min with vigorous stirring. Then, the flask was cooled instantly to room temperature by a cold water bath. Five milliliters of hexane and 15 mL of ethanol were added to the flask. The cobalt sulfide nanocrystals were washed by centrifugation at 8000 rpm for 10 min, whereas byproducts and unreacted precursors were discarded. For large-scale production of Co_9S_8 nanocrystals, all of the reactants were scaled up to 10 times in volume or in moles than the above recipe with 500 mL flask.

Counter-Electrode Fabrication. *Cobalt Sulfide Counter-Electrode.* Mo-coated glass substrate was fabricated by DC magnetron sputtering with a film thickness of 500 nm. A thin layer of Co_9S_8 was deposited by spraying coating method. The Co_9S_8 nanoink was prepared by Co_9S_8 nanocrystals dispersed in hexane with a concentration of 20 mg/mL. The nanoink was sprayed onto the FTO glass substrate (SnO_2:F glass, 8 Ω/sq) and Mo-coated glass substrate by using an airbrush (KUSING BD-130, 0.3 mm) operated at ∼15−20 psig of head pressure. Both kind of electrodes, cobalt sulfide nanocrystals on FTO glass substrate (Co_9S_8/FTO) and cobalt sulfide nanocrystals on Mo-coated glass substrate (Co_9S_8/Mo), were sintered at 350 °C in an Ar atmosphere for 2 h.

Pt Counter-Electrode. The Pt counter-electrode was prepared by screen printing process of Pt paste (in terpineol) on FTO glass substrate and reacted at 385 °C for 30 min.

Cell Assembly. In a typical preparation procedure, a 18 μm TiO_2 nanocrystalline film sensitized with dye N719 was used as photoanode. The TiO_2 film was cleaned by UV lamp for 20 min and then immersed in a 5×10^{-4} M solution of N719 dye in acetonitrile/tertbutanol (volume ratio = 1:1) for 24 h. The cells with active area of 2 cm^2 were assembled by clipping two electrodes together with a spacer between the two electrodes. The liquid electrolyte was composed of 0.05 M I_2, 0.1 M LiI, 0.6 M 1,2-dimethyl-3-propylimidazolium iodide (DMPII), and 0.5 M 4-*tert*-butylpyridine with acetonitrile as the solvent and injected into the aperture between two electrode.

Characterization and Measurement. *Characterization of Cobalt Sulfide Nanocrystals.* Cobalt sulfide nanocrystals were characterized by the following instruments: TEM, SEM, XRD, EDS, and XPS.

TEM images were obtained on JEOL JEM-1200 at an accelerating voltage of 120 kV for low resolution imaging and on a JEOL JEM-3000F at an accelerating voltage of 300 kV equipped with an Oxford INCA EDS detector for EDS analysis, respectively. SEM images were obtained on JSM-6500. XRD data were obtained by Rigaku Ultima IV X-ray diffractometer using a Cu radiation source (λ = 1.54 Å). XPS analysis was performed on ULVAC-PHI XPS.

Cyclic Voltammetry Measurement. Cyclic voltammetry (CV) was recorded with a three electrode system on a multichannel electrochemical analyzer (Bio-Logic-Science Instruments, VMP3). Pt was used as the counter electrode, and Ag/Ag^+ was used as the reference electrode. An argon-purged solution of 10.0 mM LiI, 1.0 mM I_2, and 0.1 M $LiClO_4$ in acetonitrile served as the electrolyte. CV curves were recorded in the range of 1.0 to −1.0 V at a scan rate of 20 mV/s.

Tafel Polarization Measurement. Tafel-polarization measurements were employed with an electrochemical workstation system (VMP3) in a symmetrical dummy cell. The electrolyte was as the same of the electrolyte of DSSC. The scan rate was 20 mV/s.

Photocurrent−Voltage (J−V) Characteristic Curves and EIS Measurement. The *J−V* performance of the DSSCs was measured under solar simulator (AM 1.5, 100 mW/cm^2). Electrochemical impedance spectrometer (Autolab) was employed to determine the charge transfer resistance (R_{ct}), which was taken under solar stimulation in the frequency range of 10^5−10^{-2} Hz. The spectra were fitted by the Zview software.

Conflict of Interest: The authors declare no competing financial interest.

Acknowledgment. The authors acknowledge the financial support by the National Science Council of Taiwan (NSC 102-2221-E-007-023-MY3, NSC 102-2221-E-007-090-MY2, and NSC 101-2623-E-007-013-IT), the Minitry of Economic Affairs, Taiwan (101-EC-17-A-09-S1-198), National Tsing Hua University (102N2051E1, 102N2061E1), and the assistance from Center for Energy and Environmental Research, National Tsing-Hua University. The financial support provided by Bureau of Energy (Grant No. 102-D0104) and Industrial Technology Research Institute are gratefully acknowledged.

Supporting Information Available: XRD pattern and SEM images of Co_9S_8 nanocrystal films; other photocurrent−voltage (*J−V*) plots of DSSC devices; movies (MPG) showing the fabrication of spray-deposited Co_9S_8 DSSC cathodes and various electronic devices powered by the DSSCs. This material is available free of charge *via* the Internet at http://pubs.acs.org.

REFERENCES AND NOTES

1. Watt, J.; Cheong, S.; Tilley, R. D. How To Control The Shape of Metal Nanostructures in Organic Solution Phase Synthesis for Plasmonics and Catalysis. *Nano Today* **2013**, *8*, 198–215.
2. Watt, J.; Yu, C.; Chang, S. L.; Cheong, S.; Tilley, R. D. Shape Control from Thermodynamic Growth Conditions: The Case of hcp Ruthenium Hourglass Nanocrystals. *J. Am. Chem. Soc.* **2012**, *135*, 606–609.
3. Coughlan, C.; Singh, A.; Ryan, K. M. Systematic Study into the Synthesis and Shape Development in Colloidal $CuIn_xGa_{1-x}S_2$ Nanocrystals. *Chem. Mater.* **2013**, *25*, 653–661.
4. Weintraub, B.; Wei, Y.; Wang, Z. L. Optical Fiber/Nanowire Hybrid Structures for Efficient Three-Dimensional Dye-Sensitized Solar Cells. *Angew. Chem., Int. Ed.* **2009**, *48*, 8981–8985.
5. Wei, Y.; Xu, C.; Xu, S.; Li, C.; Wu, W.; Wang, Z. L. Planar Waveguide−Nanowire Integrated Three-Dimensional Dye-Sensitized Solar Cells. *Nano Lett.* **2010**, *10*, 2092–2096.
6. Singh, A.; Coughlan, C.; Laffir, F.; Ryan, K. M. Assembly of $CuIn_{1-x}Ga_xS_2$ Nanorods into Highly Ordered 2D and 3D Superstructures. *ACS Nano* **2012**, *6*, 6977–6983.

7. Calogero, G.; Calandra, P.; Irrera, A.; Sinopoli, A.; Citro, I.; Di Marco, G. A New Type of Transparent and Low Cost Counter-electrode Based on Platinum Nanoparticles for Dye-Sensitized Solar Cells. *Energy Environ. Sci.* **2011**, *4*, 1838–1844.
8. Li, P.; Wu, J.; Lin, J.; Huang, M.; Lan, Z.; Li, Q. Improvement of Performance of Dye-Sensitized Solar Cells Based on Electrodeposited-Platinum Counter Electrode. *Electrochim. Acta* **2008**, *53*, 4161–4166.
9. Yoon, C. H.; Vittal, R.; Lee, J.; Chae, W.-S.; Kim, K.-J. Enhanced Performance of a Dye-Sensitized Solar Cell with an Electrodeposited-platinum Counter Electrode. *Electrochim. Acta* **2008**, *53*, 2890–2896.
10. Murakami, T. N.; Grätzel, M. Counter Electrodes for DSC: Application of Functional Materials as Catalysts. *Inorg. Chim. Acta* **2008**, *361*, 572–580.
11. Ramasamy, E.; Lee, W. J.; Lee, D. Y.; Song, J. S. Nanocarbon Counterelectrode for Dye Sensitized Solar Cells. *Appl. Phys. Lett.* **2007**, *90*, 173103–173103−3.
12. Wu, J.; Li, Q.; Fan, L.; Lan, Z.; Li, P.; Lin, J.; Hao, S. High-Performance Polypyrrole Nanoparticles Counter Electrode for Dye-Sensitized Solar Cells. *J. Power Sources* **2008**, *181*, 172–176.
13. Lee, W. J.; Ramasamy, E.; Lee, D. Y.; Song, J. S. Efficient Dye-Sensitized Solar Cells with Catalytic Multiwall Carbon Nanotube Counter Electrodes. *ACS Appl. Mater. Interfaces* **2009**, *1*, 1145–1149.
14. Faber, M. S.; Park, K.; Cabán-Acevedo, M.; Santra, P. K.; Jin, S. Earth-Abundant Cobalt Pyrite (CoS_2) Thin Film on Glass as a Robust, High-Performance Counter Electrode for Quantum Dot-Sensitized Solar Cells. *J. Phys. Chem. Lett.* **2013**, *4*, 1843–1849.
15. Wu, M.; Lin, X.; Wang, Y.; Wang, L.; Guo, W.; Qi, D.; Peng, X.; Hagfeldt, A.; Grätzel, M.; Ma, T. Economical Pt-Free Catalysts for Counter Electrodes of Dye-Sensitized Solar Cells. *J. Am. Chem. Soc.* **2012**, *134*, 3419–3428.
16. Li, G.; Song, J.; Pan, G.; Gao, X. Highly Pt-Like Electrocatalytic Activity of Transition Metal Nitrides for Dye-Sensitized Solar Cells. *Energy Environ. Sci.* **2011**, *4*, 1680–1683.
17. Jiang, Q.; Li, G.; Gao, X. Highly Ordered TiN Nanotube Arrays as Counter Electrodes for Dye-Sensitized Solar Cells. *Chem. Commun.* **2009**, 6720–6722.
18. Zhang, H.; Ge, M.; Yang, L.; Zhou, Z.; Chen, W.; Li, Q.; Liu, L. Synthesis and Catalytic Properties of Sb_2S_3 Nanowire-Bundle as Counter Electrode for Dye-Sensitized Solar Cells. *J. Phys. Chem. C* **2013**, *117*, 10285–10290.
19. Xin, X.; He, M.; Han, W.; Jung, J.; Lin, Z. Low-Cost Copper Zinc Tin Sulfide Counter Electrodes for High-Efficiency Dye-Sensitized Solar Cells. *Angew. Chem., Int. Ed.* **2011**, *50*, 11739–11742.
20. Gong, F.; Wang, H.; Xu, X.; Zhou, G.; Wang, Z.-S. *In Situ* Growth of $Co_{0.85}Se$ and $Ni_{0.85}Se$ on Conductive Substrates as High-Performance Counter Electrodes for Dye-Sensitized Solar Cells. *J. Am. Chem. Soc.* **2012**, *134*, 10953–10958.
21. Wang, Y. C.; Wang, D. Y.; Jiang, Y. T.; Chen, H. A.; Chen, C. C.; Ho, K. C.; Chou, H. L.; Chen, C. W. FeS_2 Nanocrystal Ink as a Catalytic Electrode for Dye-Sensitized Solar Cells. *Angew. Chem., Int. Ed.* **2013**, *52*, 6694–6698.
22. Li, G. r.; Wang, F.; Jiang, Q. w.; Gao, X. p.; Shen, P. w. Carbon Nanotubes with Titanium Nitride as a Low-Cost Counter-Electrode Material for Dye-Sensitized Solar Cells. *Angew. Chem., Int. Ed.* **2010**, *49*, 3653–3656.
23. Okumura, T.; Sugiyo, T.; Inoue, T.; Ikegami, M.; Miyasaka, T. Nickel Oxide Hybridized Carbon Film as an Efficient Mesoscopic Cathode for Dye-Sensitized Solar Cells. *J. Electrochem. Soc.* **2013**, *160*, H155–H159.
24. Wang, Z.-S.; Li, Z.; Gong, F.; Zhou, G. NiS_2/Reduced Graphene Oxide Nanocomposites for Efficient Dye-Sensitized Solar Cells. *J. Phys. Chem. C.* **2013**, *117*, 6561–6566.
25. Ghezelbash, A.; Korgel, B. A. Nickel Sulfide and Copper Sulfide Nanocrystal Synthesis and Polymorphism. *Langmuir* **2005**, *21*, 9451–9456.
26. Steinhagen, C.; Harvey, T. B.; Stolle, C. J.; Harris, J.; Korgel, B. A. Pyrite Nanocrystal Solar Cells: Promising, or Fool's Gold? *J. Phys. Chem. Lett.* **2012**, *3*, 2352–2356.
27. Cabán-Acevedo, M.; Liang, D.; Chew, K. S.; DeGrave, J. P.; Kaiser, N. S.; Jin, S. Synthesis, Characterization, and Variable Range Hopping Transport of Pyrite (FeS_2) Nanorods, Nanobelts, and Nanoplates. *ACS Nano* **2013**, *7*, 1731–1739.
28. Bai, Y.; Yeom, J.; Yang, M.; Cha, S.-H.; Sun, K.; Kotov, N. A. Universal Synthesis of Single-Phase Pyrite FeS_2 Nanoparticles, Nanowires, and Nanosheets. *J. Phys. Chem. C* **2013**, *117*, 2567–2573.
29. Beal, J. H.; Prabakar, S.; Gaston, N.; Teh, G. B.; Etchegoin, P. G.; Williams, G.; Tilley, R. D. Synthesis and Comparison of The Magnetic Properties of Iron Sulfide Spinel and Iron Oxide Spinel Nanocrystals. *Chem. Mater.* **2011**, *23*, 2514–2517.
30. Baumgardner, W. J.; Choi, J. J.; Lim, Y.-F.; Hanrath, T. SnSe Nanocrystals: Synthesis, Structure, Optical Properties, and Surface Chemistry. *J. Am. Chem. Soc.* **2010**, *132*, 9519–9521.
31. Choi, J. J.; Lim, Y.-F.; Santiago-Berrios, M. E. B.; Oh, M.; Hyun, B.-R.; Sun, L.; Bartnik, A. C.; Goedhart, A.; Malliaras, G. G.; Abruña, H. c. D. PbSe Nanocrystal Excitonic Solar Cells. *Nano Lett.* **2009**, *9*, 3749–3755.
32. Sidik, R. A.; Anderson, A. B. Co_9S_8 as a Catalyst for Electroreduction of O_2: Quantum Chemistry Predictions. *J. Phys. Chem. B* **2006**, *110*, 936–941.
33. Alonso-Vante, N. 5 Structure and Reactivity of Transition Metal Chalcogenides toward the Molecular Oxygen Reduction Reaction. In *Interfacial Phenomena in Electrocatalysis*; Springer: New York, 2011; pp 255−300.
34. Geller, S. Refinement of The Crystal Structure of Co_9S_8. *Acta Crystallogr.* **1962**, *15*, 1195–1198.
35. Rao, C.; Pisharody, K. Transition Metal Sulfides. *Prog. Solid State Chem.* **1976**, *10*, 207–270.
36. Wenk, H.-R.; Bulakh, A. *Minerals: Their Constitution and Origin*; Cambridge University Press: Cambridge, 2004.
37. Liu, Q.; Zhang, J.-Y. A General Synthesis of Co_mS_n (Co_9S_8, Co_3S_4, and $Co_{1-x}S$) Hierarchical Microspheres with Controllable Homogeneous Phases. *CrystEngComm* **2013**, *15*, 5087–5092.
38. Chen, G.; Ma, W.; Zhang, D.; Zhu, J.; Liu, X. Shape Evolution and Electrochemical Properties of Cobalt Sulfide *via* a Biomolecule-Assisted Solvothermal Route. *Solid State Sci.* **2012**, *17*, 102–106.
39. Yin, Y.; Erdonmez, C. K.; Cabot, A.; Hughes, S.; Alivisatos, A. P. Colloidal Synthesis of Hollow Cobalt Sulfide Nanocrystals. *Adv. Funct. Mater.* **2006**, *16*, 1389–1399.
40. Kung, C.-W.; Chen, H.-W.; Lin, C.-Y.; Huang, K.-C.; Vittal, R.; Ho, K.-C. CoS Acicular Nanorod Arrays for the Counter Electrode of an Efficient Dye-Sensitized Solar Cell. *ACS Nano* **2012**, *6*, 7016–7025.
41. Zhang, X.; Liu, Q.; Meng, L.; Wang, H.; Bi, W.; Peng, Y.; Yao, T.; Wei, S.; Xie, Y. In-Plane Coassembly Route to Atomically-Thick Inorganic-Organic Hybrid Nanosheets. *ACS Nano* **2013**, *7*, 1682–1688.
42. Niu, J.; Xu, W.; Shen, H.; Li, S.; Wang, H.; Li, L. S. Synthesis of CdS, ZnS, and CdS/ZnS Core/Shell Nanocrystals Using Dodecanethiol. *Bull. Korean Chem. Soc.* **2012**, *33*, 393–397.
43. Singh, A.; Geaney, H.; Laffir, F.; Ryan, K. M. Colloidal Synthesis of Wurtzite Cu_2ZnSnS_4 Nanorods and Their Perpendicular Assembly. *J. Am. Chem. Soc.* **2012**, *134*, 2910–2913.
44. Kuzuya, T.; Itoh, K.; Sumiyama, K. Low Polydispersed Copper-Sulfide Nanocrystals Derived from Various Cu−Alkyl Amine Vomplexes. *J. Colloid Interface Sci.* **2008**, *319*, 565–571.
45. Alstrup, I.; Chorkendorff, I.; Candia, R.; Clausen, B. S.; Topsøe, H. A Combined X-Ray Photoelectron and Mössbauer Emission Spectroscopy Study of The State of Cobalt in Sulfided, Supported, and Unsupported Co-Mo Catalysts. *J. Catal.* **1982**, *77*, 397–409.
46. Wang, Z.; Pan, L.; Hu, H.; Zhao, S. Co_9S_8 Nanotubes Synthesized on the Basis of Nanoscale Kirkendall Effect and Their Magnetic and Electrochemical Properties. *CrystEngComm* **2010**, *12*, 1899–1904.
47. Zhou, Y. X.; Yao, H. B.; Wang, Y.; Liu, H. L.; Gao, M. R.; Shen, P. K.; Yu, S. H. Hierarchical Hollow Co_9S_8 Microspheres: Solvothermal Synthesis, Magnetic, Electrochemical, and Electrocatalytic Properties. *Chem.—Eur. J.* **2010**, *16*, 12000–12007.

48. Schmidt, T.; Gärtner, F.; Assadi, H.; Kreye, H. Development of A Generalized Parameter Window for Cold Spray Deposition. *Acta Mater.* **2006**, *54*, 729–742.
49. Chen, J.; Li, K.; Luo, Y.; Guo, X.; Li, D.; Deng, M.; Huang, S.; Meng, Q. A Flexible Carbon Counter Electrode for Dye-Sensitized Solar Cells. *Carbon* **2009**, *47*, 2704–2708.
50. Popov, A. I.; Geske, D. H. Studies on The Chemistry of Halogen and of Polyhalides. XIII. Voltammetry of Iodine Species in Acetonitrile. *J. Am. Chem. Soc.* **1958**, *80*, 1340–1352.
51. Wang, M.; Anghel, A. M.; Marsan, B. t.; Cevey, Ha, N.-L.; Pootrakulchote, N.; Zakeeruddin, S. M.; Grätzel, M. CoS Supersedes Pt as Efficient Electrocatalyst for Triiodide Reduction in Dye-Sensitized Solar Cells. *J. Am. Chem. Soc.* **2009**, *131*, 15976–15977.
52. Hsu, C.-P.; Lee, K.-M.; Huang, J. T.-W.; Lin, C.-Y.; Lee, C.-H.; Wang, L.-P.; Tsai, S.-Y.; Ho, K.-C. EIS Analysis on Low Temperature Fabrication of TiO_2 Porous Films for Dye-sensitized Solar Cells. *Electrochim. Acta* **2008**, *53*, 7514–7522.
53. Subramanian, A.; Wang, H.-W. Effects of Boron Doping in TiO_2 Nanotubes and The Performance of Dye-Sensitized Solar Cells. *Appl. Surf. Sci.* **2012**, *258*, 6479–6484.
54. Tang, Y.; Pan, X.; Zhang, C.; Dai, S.; Kong, F.; Hu, L.; Sui, Y. Influence of Different Electrolytes on The Reaction Mechanism of a Triiodide/Iodide Redox Couple on the Platinized FTO Glass Electrode in Dye-Sensitized Solar Cells. *J. Phys. Chem. C* **2010**, *114*, 4160–4167.